

The Effect of Battery Potential and Charge Rate on the Decomposition Reaction on the Anode Electrode of Lithium Ion Polymer Battery

Victor Agubra¹, Jeffrey W. Fergus¹, Rujian Fu², Song-yul Choe²

¹Materials Research and Education Center, 275 Wilmore Laboratories, Auburn University, Auburn, AL 36849, USA

²Department of Mechanical Engineering, Wiggins, Auburn University, Auburn, AL 36849, USA

Abstract

The breakdown of the protective solid electrolyte interface (SEI) layer on the anode electrode can initiate further electrolyte decomposition reaction and result in the formation of a non-uniform layer of electronically insulating reaction products on the graphite particles. The results from this study indicated that raising the state of charge (SOC) increased the rate of the electrolyte decomposition side reaction to form a thick deposit layer. The deposit surface layer formed at the electrode/electrolyte interface increased the interfacial charge transfer resistance and rise in the overall batteries impedance. A direct correlation between the capacity fade during cycling and the deposit layer growth was established. Analysis of the anode and the deposit layer showed an increasing amount of lithium in the deposit layer as well as “trapped” lithium in the graphite crystal structure as the batteries were aged at higher SOC.

1. Introduction

The high energy/ power density (typically twice that of the standard nickel-cadmium batteries), and excellent cycle life of the lithium ion battery (LIB) have positioned it as the preferred portable energy source for most consumer appliances and in the automotive industry for electric vehicles (EV) and hybrid electric vehicles (HEV). However, several reported batteries failures during application have raised concerns about their safety during application. The performance of the LIB depends on the development of materials for the various components (1-3). The degradation of these components during operation adversely affects the energy delivery of the LIB. Mechanisms such as loss of accessible lithium ions, degradation of electrodes, binder and current collectors, decomposition of the electrolyte to form an insoluble film between electrode and electrolyte interface have been reported as some the main contributing factors to capacity fade (4-6).

Passivation of the electrode from electrolyte decomposition products is also of concern. In particular, the reduction of the electrolyte salt, LiPF_6 , into a strong Lewis acid PF_5 (7), which undergoes a ring-opening reaction with ethylene carbonate (EC) and in the presence of the Li^+ initiates the formation of insoluble organic and inorganic lithium species on the surface of the anode electrode (SEI layer). A robust SEI layer prevents further electrolyte solvent reduction on the carbon electrode. However, the metastable

species ROCO_2Li within the SEI layer can decompose into more stable compounds – Li_2CO_3 and LiF at elevated temperature (8). The products of this reaction create a porous SEI structure that exposes the graphite surface to more electrolyte decomposition reaction, resulting in the formation of a variety of layers on the electrode surface (9). These deposited layers lead to the loss/consumption of recyclable lithium ions at electrode/electrolyte interface. In addition, the formed surface layer on the anode clogs the pores on the carbon anode electrode that may limit the accessibility of lithium ions into the anode (10, 11) leading to an increased in the charge transfer/Ohmic resistance of the battery (12-14). This surface layer affects the electrochemical reaction on the surface of the anode and thus impacts on the reversible capacity of the LIB.

In this article, a quantitative analysis the effect of the state of charge (SOC) on the growth of the deposit layer is presented. This relationship is important for understanding how charging protocols are related to performance degradation.

2.0 Experimental

2.1 Battery Chemistry

The batteries used in this study were commercially available pouch-type lithium ion polymer batteries (LiB) from battery manufacturer LGChem with a Li (Mn, Ni, Co) O_2 cathode and the anode material is made of 100% carbon with polyvinylidene fluoride (PVDF) as the binding material. The current collectors of anode and cathode electrode were aluminum and copper current respectively. The electrolyte was an organic salt, LiPF_6 , with co-solvents of ethylene carbonate (EC), and dimethyl carbonate (DMC). The nominal capacity of each battery is 15.7 Ah with an operating voltage level between 2.5 to 4.15 V.

2.2 Cycling Test

The charge/discharge cycles were performed using a in-house designed test station comprised of a programmable charging system, a programmable electronic load system, a data acquisition system that are controlled by LabVIEW™ residing in a PC. The testing system allowed for the input of various charging conditions, such as C-rate, state of charge (SOC), and was located in an environmental chamber to allow for control of the external temperature. The batteries were charged by a constant current-constant voltage (CC-CV) charging protocol at room temperature. In each cycle, the cell was discharged with a constant current until the terminal voltage decreased to the voltage corresponding to the desired lower SOC and then charged with a constant current up to the voltage corresponding to the upper SOC followed by a constant voltage (CV) charge. A 4C charge and discharge current were used to accelerate the aging process.

After every 20 cycles, a 1C discharge-resting-charge profile was applied to the cell to measure its capacity. The capacity (Q_{max}) was calculated by integrating the current when the cell was being discharged from 100% to 0% SOC using 1C current (15.7A) at room temperature. The Q_{max} data for each battery were recorded every 20 cycles. The battery

was rested for 10 minutes before and after the Q_{\max} measurement. The SOC levels; 5-70%, 15-80% and 25-90% were chosen to maintain a constant capacity of 65%. The pre-test terminal voltage for the desired SOC was determined by coulomb counting.

2.3 Electrochemical Impedance Spectroscopy (EIS)

A Gamry electrochemical impedance spectroscopy (EIS) framework in galvanostatic mode was used to apply different frequencies (1 mHz to 1 kHz) of small AC excitation current (1A) to the battery and voltage responses were collected at 25°C. A bipolar power supply was used to amplify the signal from EIS signal board. The measured impedances of the batteries were fit using the equivalent circuit model shown in Figure 1 to extract parameters such as the SEI film resistance, the Ohmic resistance, the charge transfer resistance, the double layer capacitance and Warburg impedance of the battery. In the model, R_0 is the ohmic resistance caused by electrolyte, deposit layer, separator, current collector and electrode, which equals to the left intercept between impedance spectrum and the x-axis at high frequency ($\approx 1\text{kHz}$) (15). R_{sei} and C_1 indicate SEI resistance and capacitance at anode, which dominate the shape of the first semi-circle in high frequency domain from 1kHz to several Hz (16). While R_c and C_2 indicate charge transfer resistance and double layer capacitance, respectively. They affect the shape of the second semi-circle, which is less obvious in the lower frequency range (several Hz to several mHz) (17). On the other hand, W_a is the Warburg admittance that represents ion diffusion in the electrolyte (17) and C_3 is the intercalation capacitance that indicates the process of ion intercalation (16). Both W_a and C_3 dominate the impedance spectrum in the low frequency region ($< \text{several mHz}$). In this only the Ohmic, SEI and the charge transfer resistances are of interest.

2.4 Materials Postmortem Analysis

After cycling and measuring the battery capacity and impedance, the battery was discharged to 0% SOC (2.5V) and dismantled in an argon atmosphere in glove box. The anode electrodes were harvested, cleaned in DMC and dried in desiccator. A quantitative analysis of the thickness of the formed surface layer was carried out by taking a cross sectional view (the samples were mounted on an epoxy and the edges were polished) of the deposited surface layer and measuring its thickness on an image obtained using a scanning electron microscope (SEM) (Figure 1).

The electrodes with side reaction deposit were selected by visual examination. A total of eight electrodes (out of 13) were selected from each battery to represent the range of the amount of deposit layer. Specifically four electrodes with large amounts of deposit and four with small to medium amounts of deposits were analyzed. For each of the eight (8) samples, six different deposit thicknesses were measured. The thickness of the deposited layer for each battery was calculated by taking the mean value of the 48 measured thicknesses.

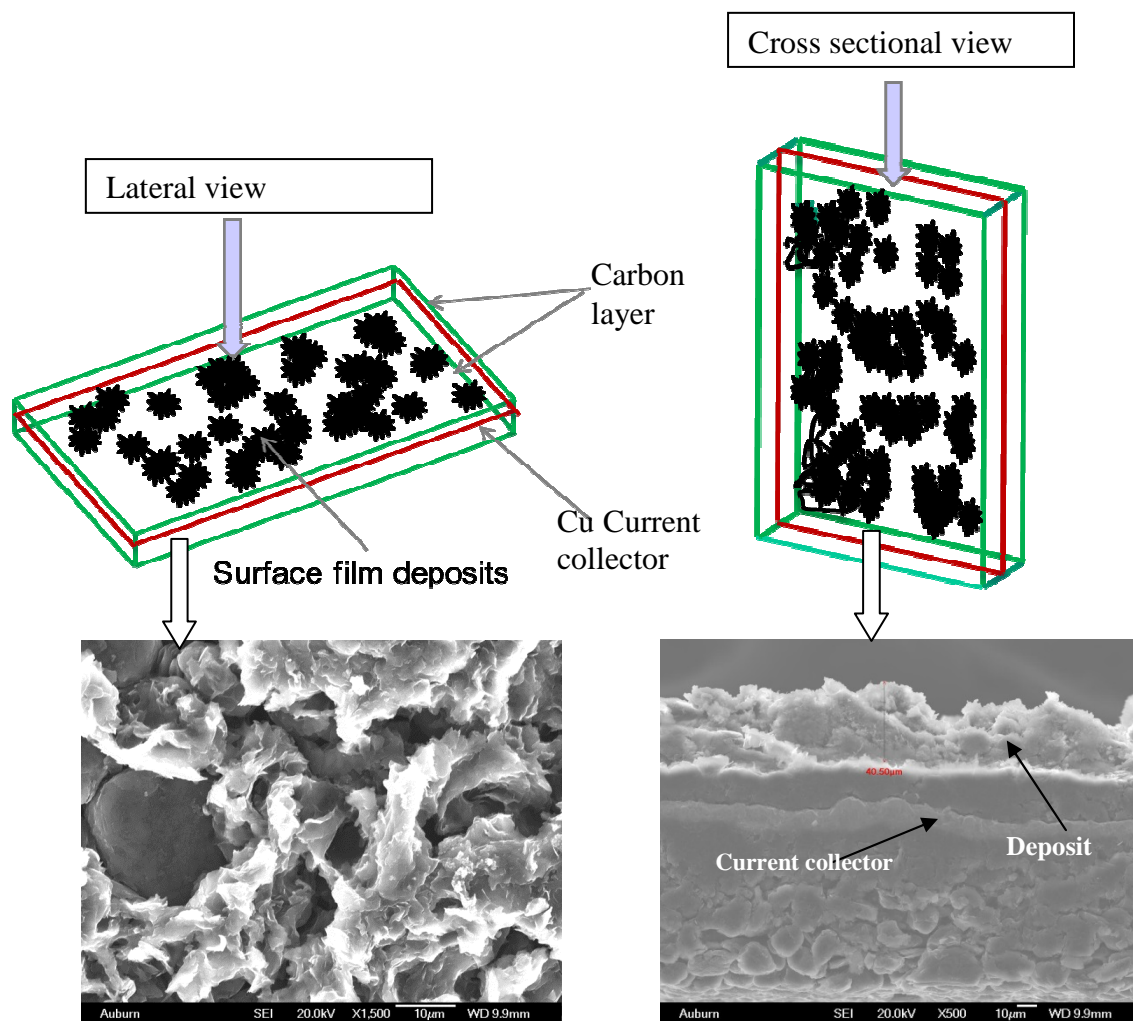


Figure 1: Lateral and cross sectional views of the deposit layer on the anode

X-ray diffraction (XRD) spectra for the graphite anode electrodes were obtained using a Bruker D8 to investigate the changes in the graphite crystal structure and the formation of new phases. The composition of the surface film was analyzed using the Bruker optics Fourier transformed infra-red spectroscopy equipped with single-reflection attenuated total reflection (ATR) accessory in absorbance mode.

3.0 Results and Discussion

3.1 Electrochemical

The measured Q_{\max} (capacity fade) values of the batteries for up to 600 cycles are plotted in Figure 2. The Q_{\max} values for both 25%-90% and 15%-80% SOC levels were similar and loss about 17% the capacity after 600 cycles, while 5%-70% SOC lost only about half as much capacity (7.8%). To elucidate the causes of these effects of cell potential (*i.e.* SOC) on capacity fade, materials analysis of the harvested anode electrode were carried out.

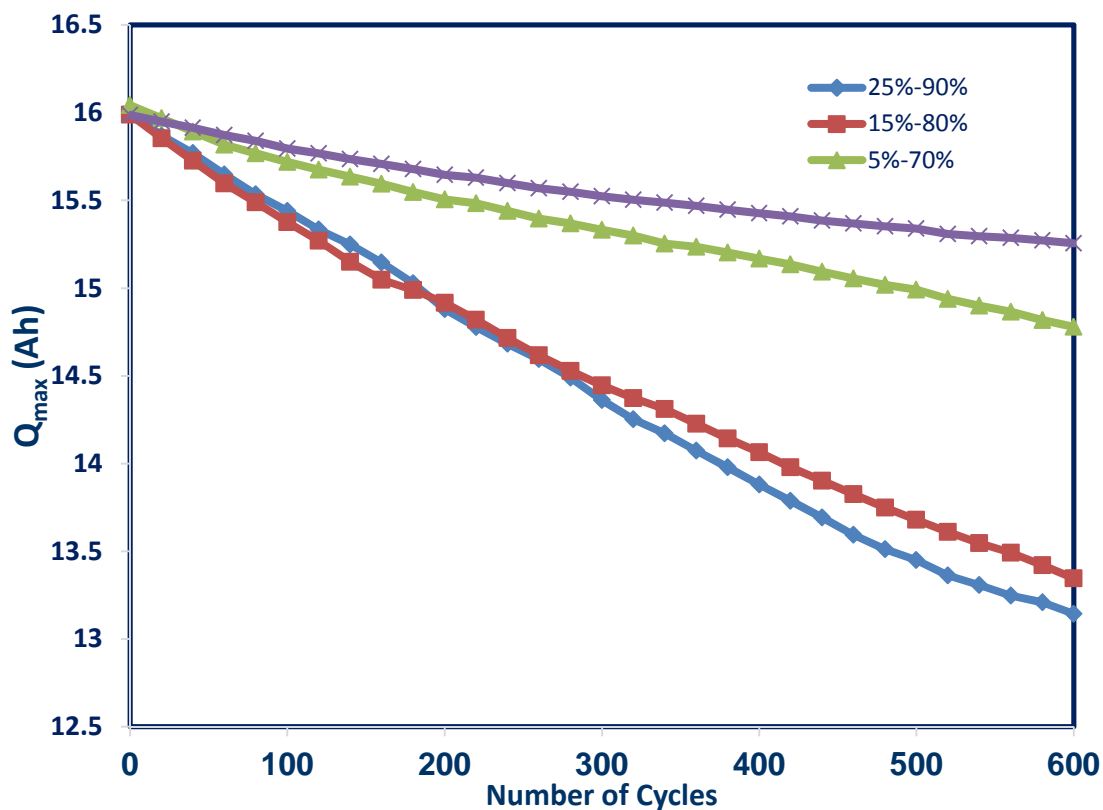


Figure 2: Capacity fade as a function of the state of charge for the batteries aged at different SOC ranges

3.2 Anode Electrode Materials Characterization

3.2.1 Deposit layer formation. SEM micrographs of the surface morphology of deposit layer on electrodes after aging are shown in Figure 3. The highly reactive solvent electrolyte, ethylene carbonate (EC), will undergo a one electron reduction reaction and was preferably solvated over DMC solvent because of its high dielectric constant and polarity (18).

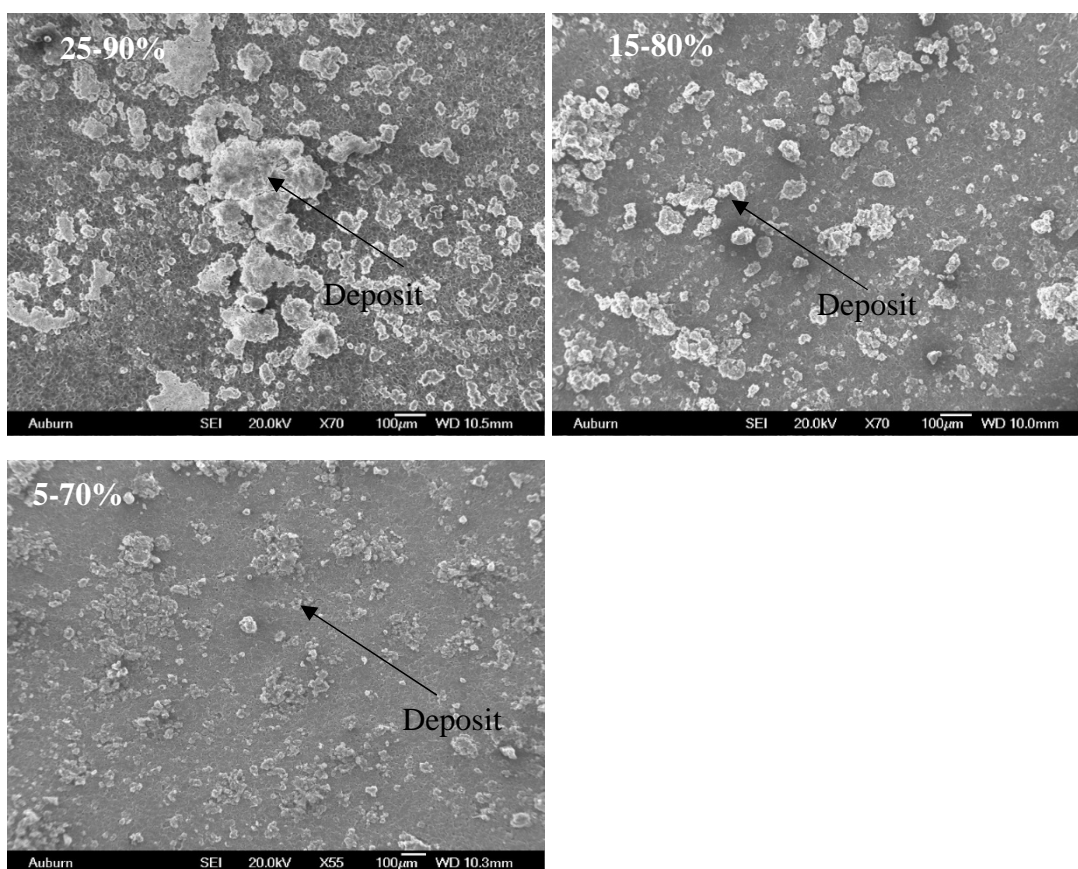


Figure 3: Distribution of deposit layer on the electrode surface for the aged electrode at different SOCs

The electrolyte decomposition process was initiated during the intercalation of Li^+ into the graphite structure, where electron transfer from the electrode to the electrolyte salt molecule initiates an autocatalytic process to produce a toxic alkyfluorophosphates, a Lewis acid and lithium fluoride as shown in equation 1.



The Lewis acid PF_5 can react further with impurities of water or alcohol (Eq. 2 and 3) in solution to produce HF and POF_3 .



These Lewis acids trigger the ring opening and bond breaking of ethylene carbonate (EC) molecules (Eq. 4) to form various species on the surface of the electrode.



In particular, the decomposition species of POF_3 and PF_6^- from LiPF_6 reduction can react with the EC molecules to produce $\text{CH}_2\text{FCH}_2\text{OCOOPF}_2\text{O}$ and CO_2 in reaction Equation 5, on the other hand, POF_3 and anion PF_6^- can also simultaneously attack the EC molecule to form the anion $\text{CH}_2\text{FCHOCOOPF}_3\text{O}^-$ and a Lewis acid PF_5 as shown in reaction equation 6.



The EC reduction process continue to produce a Lewis acid or salt anion (Eq. 7) at each subsequent reduction step that perpetuate the electrolyte reduction process.



At high SOC, these electrolyte decomposition reactions resulted in the formation and growth of the deposit layer on the surface of the graphite electrode (Figure 3) to form non-uniform agglomerates. The presence of these reaction products on the surface could block the pores of the anode electrode and retard the intercalation kinetics of the carbon anode (10). Figure 3 shows that the sizes and amounts of these agglomerates were dependent upon SOC (higher for the higher SOC), which could be due to the increased electrolyte decomposition at the higher potential during charging. At the low SOC level 5% -70%, the deposit layers were isolated. The separator removed from the cells tested from 25% to 90% SOC was dryer than those tested at 5% to 70% SOC, which was an indication of the depletion of electrolyte used in the decomposition reaction process.

3.2.2 Effects of Deposit Layer. Lithium ion batteries electrodes employ particles with pores to increase the active area between the electrolyte and the electrode to facilitate the electrochemical reaction process. A side reaction deposit layer on the surface of the active carbon materials will therefore block the electrode pores and also decrease the active surface area of the electrode, both of which can increase in the overall battery impedance.

Nyquist plots of the experimental impedance spectroscopy along with the equivalent model fits results for the different SOC levels are shown in Figure 5. The plots consist of two parts, a semicircle and a linearly increasing slope. The radius of the semicircle is attributed to the SEI resistance, while the slope is attribute to diffusion of ions in solid. The increase in radius of the semicircles with cycling implies a growth of the SEI layer and the amount of this growth was larger for higher SOC levels. The high frequency intercept, which corresponds to the ohmic resistance, increases with cycling due to the decrease in ionic conductivity of the electrolyte, caused by electrolyte compositional changes through the depletion conducting species (19). The overall battery impedance is comprised of many specific battery component/interface resistances; the Li^+ charge transfer resistance between graphite/electrolyte interface (R_c), the ohmic resistance (R_o) and the SEI layer resistance (R_{sei}).

To extract these resistances, the equivalent circuit model shown in Figure 4 was used to extract parameters that represent different electrochemical properties of the battery. The extracted parameters of resistances are plotted in Figure 6. The resistances tend to increase with increasing SOC level. The increase in the charge transfer resistance was the largest, which was attributed to the formation of a thicker deposit layer on the graphite particles.

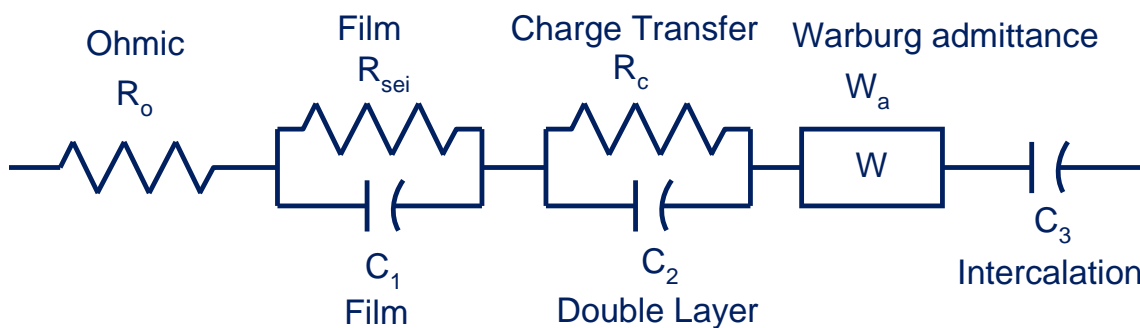


Figure 4: Equivalent circuit model schematic diagram

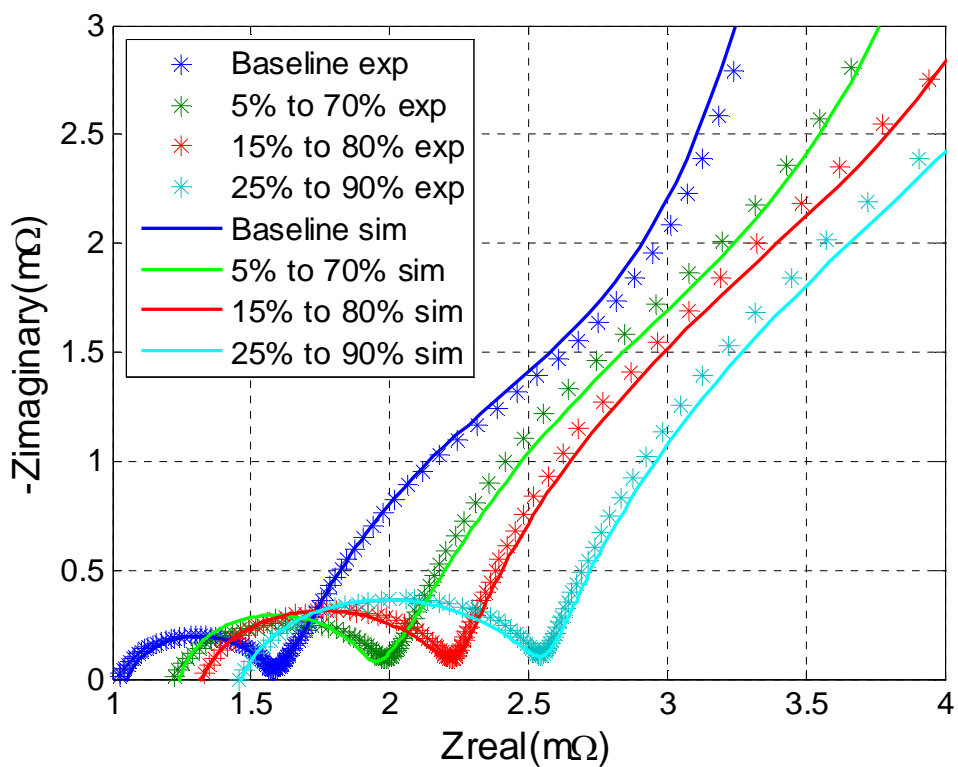


Figure 5: Comparison of Impedance for the aged batteries cycled at the various SOC's

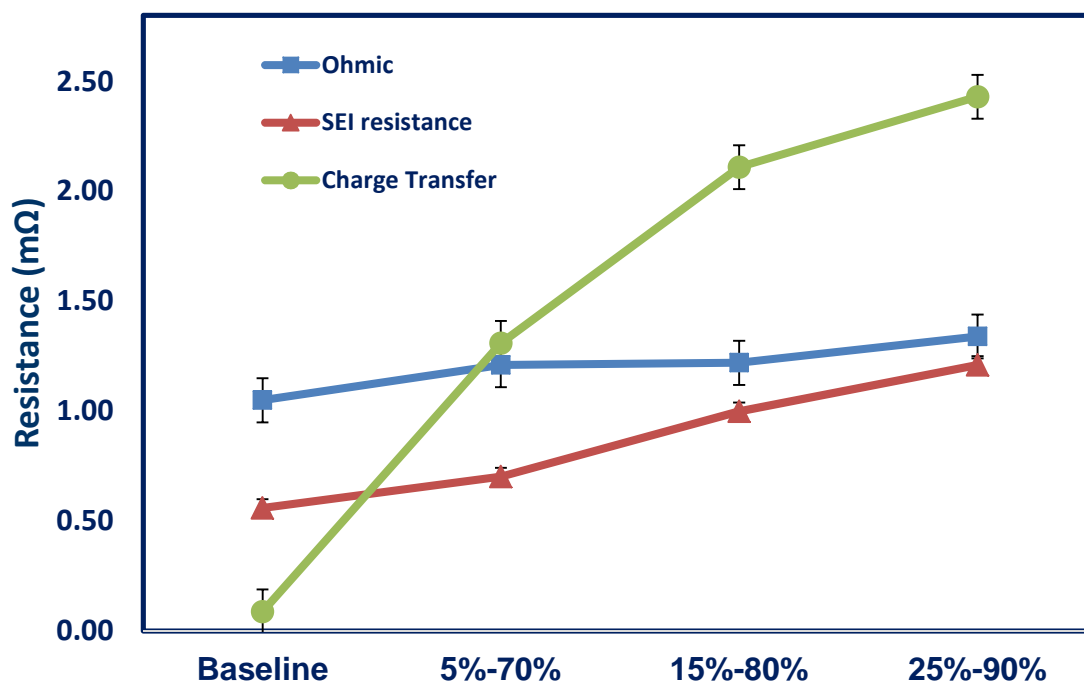


Figure 6: Resistance of the aged batteries extracted from the equivalent circuit model at different SOC

The thicknesses of the deposit layer observed among the different SOC levels was measured from cross sectional views of the anode electrode as shown in Figure 1 and the results are plotted in Figure 7. The measured deposit layer thickness increases with SOC level. The growing deposit layer for the high SOC range created a barrier for the charge transfer at the graphite /electrolyte interface (20) and cause the observed increased in charge transfer resistance and to the overall battery impedance rise.

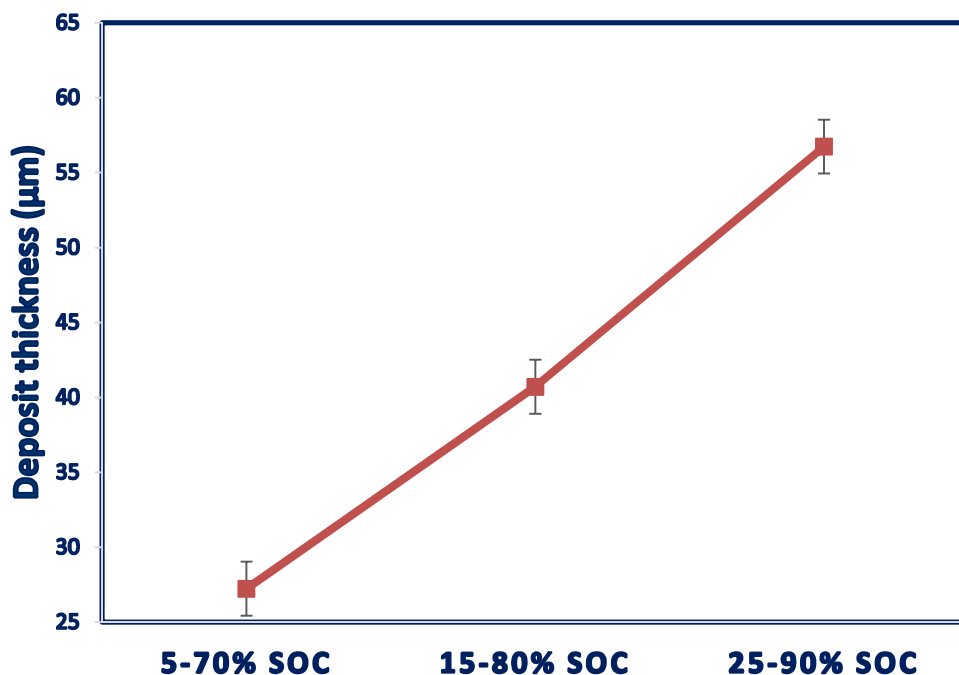


Figure 7: Deposit layer thickness form on the anode for the different state of charge

3.3.4 Composition of the Deposited Layer. The XRD spectra for the anode electrode showed a peak pattern associated with carbon and the copper current collector as shown in the Figure 8. The aged anode had a new phase (at 64°), in addition these set of peaks for the carbon and the copper current collector. This additional phase emanated from the surface layer from the electrolyte decomposition products and was attributed to the presence of the species LiF.

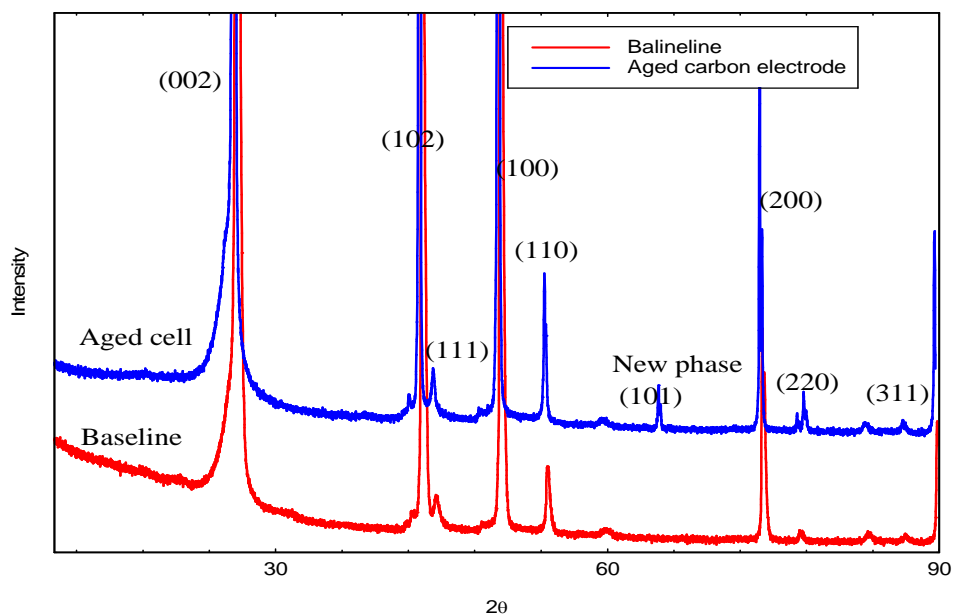


Figure 8: X-ray diffraction spectra for aged and baseline for the anode electrode

The deposit layer was analyzed further with FTIR to identify the surface compounds constituting the deposit layer. As shown in Figure 9, the absorption bands at 1750 cm^{-1} represent the stretching vibration of C=O in EC, while those at 1300 cm^{-1} and 1450 cm^{-1} are the asymmetric stretching vibration of the C-O-C and CH_2 bending vibration of decomposition products of the electrolyte solution, respectively (21). The main chemical constituents of the SEI layer in the LiPF_6 -EC/DMC solution are ROCO_2Li and Li_2CO_3 (22), which generally have spectra at 1600 cm^{-1} and 1300 cm^{-1} for ROCO_2Li and 860 cm^{-1} and 1375 cm^{-1} for Li_2CO_3 . The FTIR analysis indicated that the chemical constituents of the deposited surface film layer are the same as those in the SEI layer from the electrolyte decomposition reaction lithium on the surface of the anode electrode.

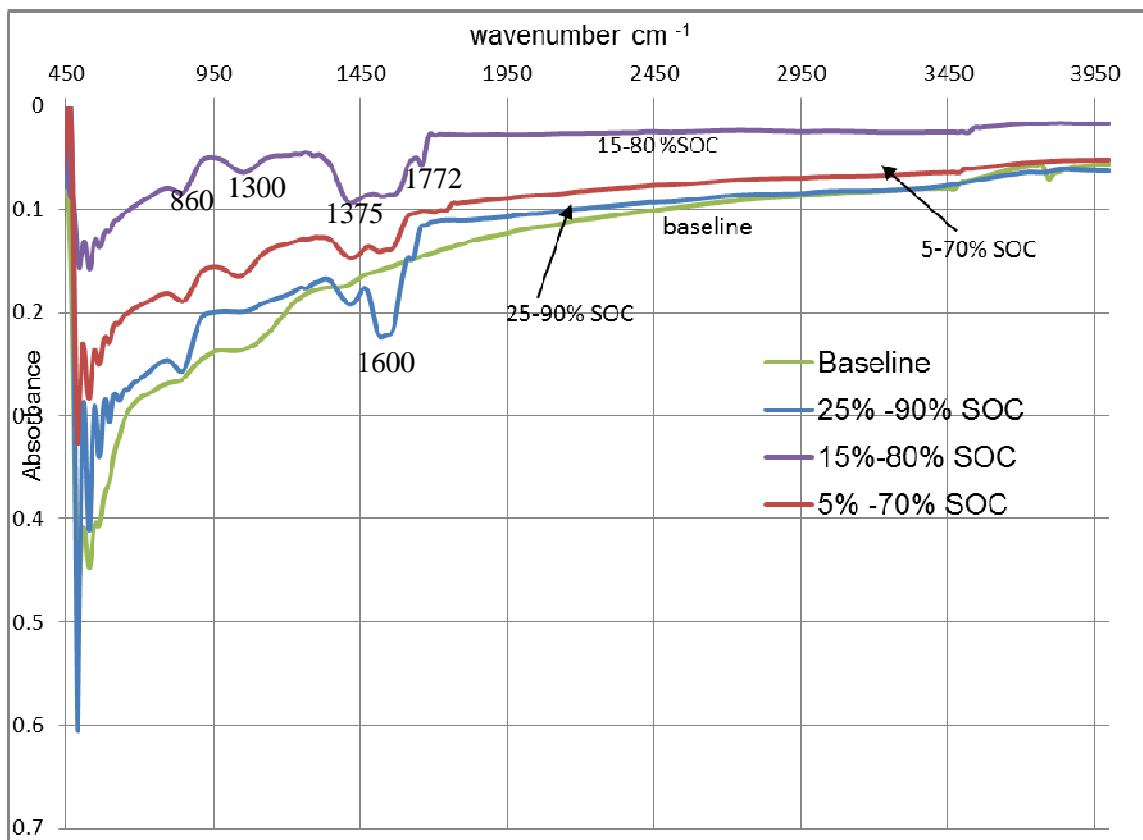


Figure 9: FTIR of surface compounds of the deposit surface layer

The insertion and de-insertion of lithium into the layered graphite structure led to volume change of the graphite anode which tends to increase the d -spacing between the graphene layers. To investigate this, further analysis of the (002) peak (Fig. 10) was undertaken to understand the possible structure changes in the carbon structure for the aged anode.

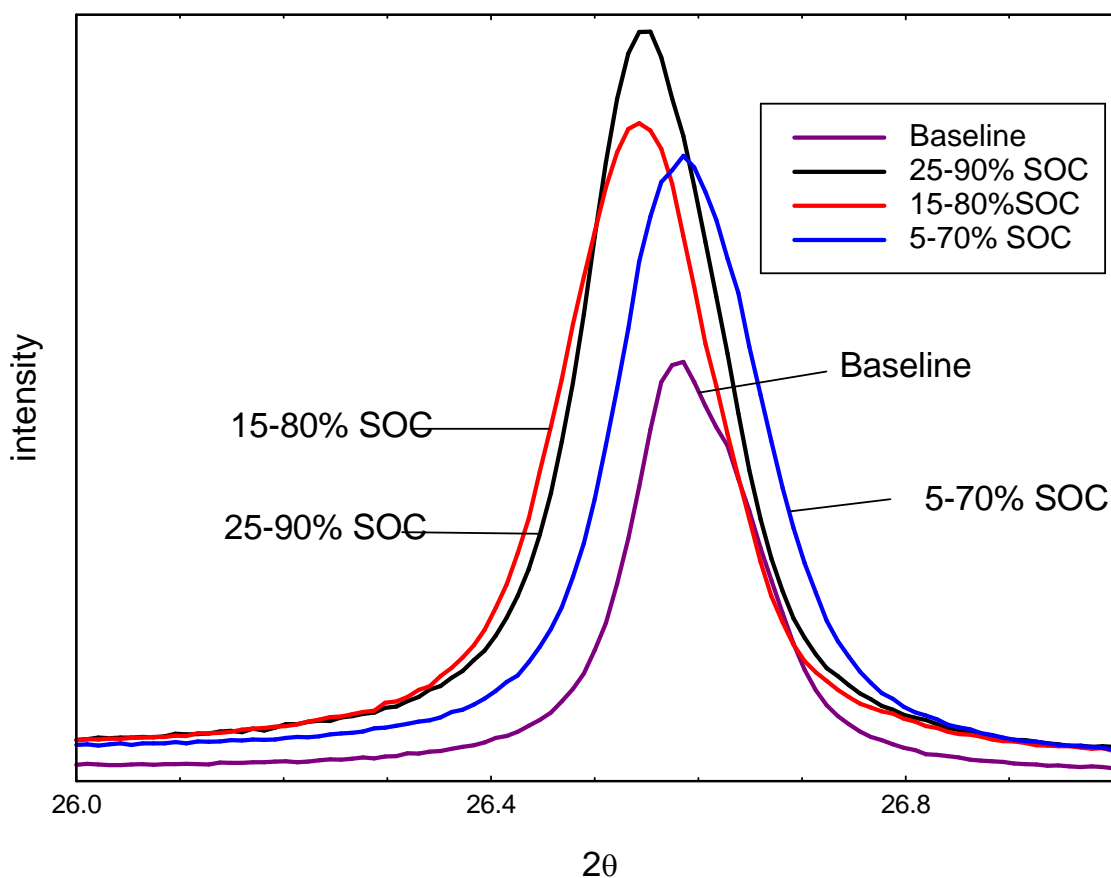


Figure 10: X-rays diffraction of the 002 peak for aged cells at various states of charge and baseline anode electrode

All the cells were discharged to 0% SOC (2.5V), which does not correspond to 0% Li in the crystal structure of the graphite so some amount of lithium would remain in the graphite structure. A total removal of the lithium content in the graphite structure would require a greater amount of energy to re-intercalate lithium back into the crystal structure. The shifts of the (002) peak to lower $2\theta^\circ$ for the 25-90% SOC and 15-80% SOC relative to the baseline, implies that some lithium remained in the graphite structure after discharge. Additionally, peak broadening was observed and indicated a range of lithium content in the graphite. The (002) peak for both the baseline and the aged had a shoulder, that was de-convoluted into two separate peaks using the Lorentz area function (Fig. 11). This implied that, for the graphite structure, two d-spacing, or a range of d-spacing, were present, which indicate that some particles had higher lithium content while other had low lithium content in the graphite electrode matrix.

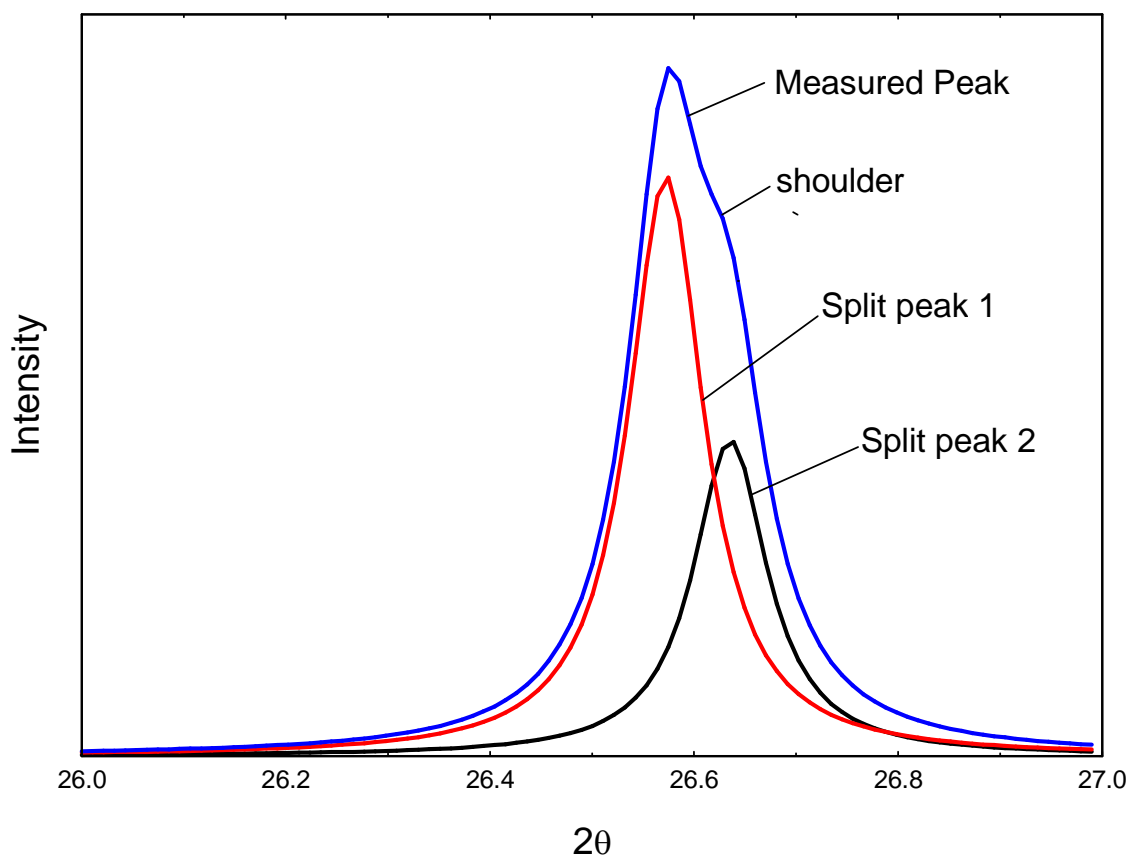


Figure 11: De-convoluted peaks for the shoulder on the baseline (002) peak

This lithium content in the graphite can be calculated from the lattice parameter and is plotted for each of the aging conditions and the baseline in Figure 12. The increase in the lithium content in the graphite layer for the aged anodes relative to the baseline indicates that some of the lithium was “trapped” in the graphite crystal structure after the discharge cycle. In the ideal case, the same level of lithium is expected to be in graphite layers for both the aged and the baseline electrode at the end of each discharged cycle. The lower d_{002} values corresponding to the lower lithium content is expected not to differ from those of the baseline graphite anode. For the case of 70% and 80% SOC cycled batteries, the lower lithium content was statistically the same as those of the baseline with the uncertainty of $\pm 0.014\%$. However, for the high SOC (i.e. 25-90%), the lower lithium content significantly differ from that of the baseline. The reason for this difference could not be readily explained, but is believed to be related to the thick deposit layer ($52\mu\text{m}$) formed on the graphite particle surface. The increasing amount of lithium residing in the deposit layer as the batteries were aged at higher SOC together with trapped lithium in the graphite layers led to loss / isolation of recycling lithium taking part in the electrochemical process. The high amount of “trapped” recyclable lithium for batteries cycled at high SOC was also directly related to the capacity fade for these cells as observed in Figure 2.

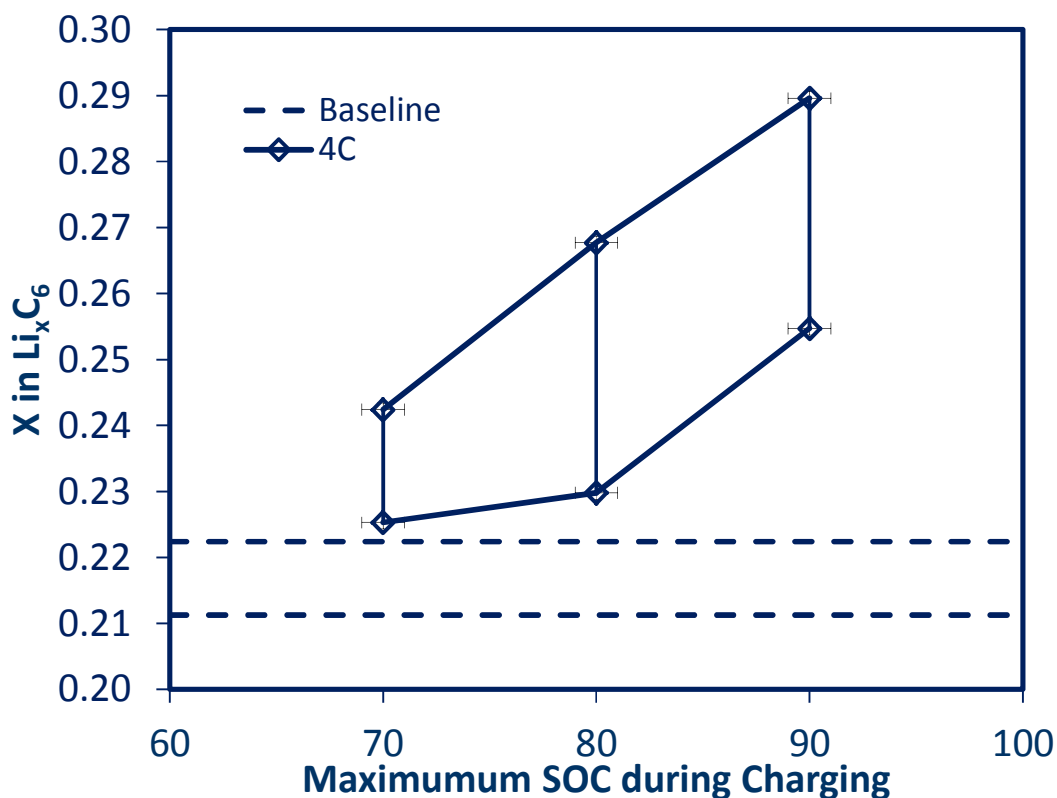


Figure 12: comparison of lithium content x in Li_xC_6 for the different SOC

4.0 Conclusion

Cycling the lithium ion batteries at high SOC level resulted in formation of thick deposit surface layer from side reaction of electrolyte decomposition. The surface layer deposited on the surface of the porous graphite electrode resulted in increased overall battery impedance due primarily to the increase in charge transfer resistance. There was a direct link between the capacity fade during cycling and the progressive build-up of the deposit layer on the anode surface. There was also an increased amount of the lithium content that was “trapped” in the graphite crystal structure after the discharge cycle.

Reference

1. M.S Whittingham, MRS Bull, **33(4)**, 411-419 (2008).
2. A. Patil, V. Patil, W.D. Shin, J. W.Choi , D. S. Paik, J. Yoon, Mater. Res. Bull, **43**, 1913-1942 (2008)
3. A.K. Shukla, T.P. Kumar, Curr. Sci. **94**, 314-331, (2008)
4. M. Dolle, L. Sannier, B. Beaudion, M. Trentin, J. Electrochem. Soc. **5**, A286 (2002)
5. M. Wolfgang, C. Lu, P. Novak, J. Electrochem. Soc. **158**, A1478(2011)
6. N.N. Sinha, T.H. Marks, H.M. Dahn, A.J. Smith, J.C. Burn, D.J. Coyle, J.J. Dahn, J.R. Dahn, J. Electrochem. Soc. **159**, A1672 (2012)
7. W. Li, C. Champion, L. B. Lucht, B. Ravdel, J. Dicarlo, K.M Abraham, J. Electrochem Soc. **152**, A1361 (2005)
8. S.B. Lee and S. Pyun, Carbon, **40**, 2333 (2002)
9. M.D. Levi, C. Wang, J.S. Gnanara, D. Aurbach, J. Power Sources, **119**, 538 (2003)
10. J.P. Fellner, G.J. Loeber, S.S. Sandhu, J. Power Sources, **81**, 867- 871, (1999)
11. M.C. Smart, B.V.Ratnakumar, S. Surapudi, Y. Wang, X. Zhang, S.G.Greenbaum, A. Hightower, C.C. Ahn, B. Fultz, J. Electrochem. Soc., **46**, A3963 (1999).
12. P.L.Moss, G. Au, E.J. Plichta, P. J. Zheng, J. Electrochem. Soc., **157(1)**, A1, (2010)
13. G. Sarre, P. Balanchard, M. Broussely, J. Power Sources, **127**, 65-712, (2004)
14. N.N. Sinha, A.J. Smith, J.C. Burns, J. Gaurav, K.W. Eberman, E. Scott, J.P. Gardner, J.R. Dahn, J. Electrochem. Soc. **158**, A1194, (2011)
15. P. Moss, G. Au, E. Plichta, J. Zheng, J. Electrochem. Soc. **157**, A1(2010)
16. G. Ning, B. Haran, B. Popov, J. Power Sources **117**, 160 (2003)
17. R. Bouchet, S. Lascaud, M. Rosso, J. Electrochem. Soc. **150**, A1385 (2003)
18. P.Novak, M. Lanz, D. Allia, B. Rykart, J. Paniz, O. Haas, J. Power Sources, **97**, 39–46, (2001).
19. L. E Ouatani, R. Dedryvère, J.-B. Ledeuil, C. Siret, P. Biensan, J. Desbrières, D. Gonbeau, J. Power Sources, **189**, 72–80, (2009)
20. B. Xu, M. S. Wu, G. Liu, and C. Y. Ouyang, J. Appl. Phys. **111**, 124-325, (2012)
21. S.I Pyun, Y.G Ryu, J. Electroanal. Chem. **455**, 11 (1998)
22. M. Masaki, K. Dokko, K. Kanamura, J. Power Sources, **177**, 184 (2008)
23. J. R. Dahn, R. Fong, M.J Spoon, Physical Review B, **42**, 6424-3432 (1990)